Journal of Colloid and Interface Science 699 (2025) 138156

Contents lists available at ScienceDirect

Journal of Colloid And Interface Science

journal homepage: www.elsevier.com/locate/jcis

Synergistic structural engineering of donor–acceptor–acceptor type conjugated microporous polymers as photocatalysts for boosting sunlight-driven hydrogen evolution

Ahmed F. Saber [a,b,1], Huei-Ting Liao [a,1], Pei-Jung Li [a], Ya-Fan Chen [a], Levannie Mabuti [a], Shiao-Wei Kuo [a], Johann Lüder [a,c], Ahmed F.M. EL-Mahdy [a,*]

[a] Department of Materials and Optoelectronic Science, National Sun Yat-Sen University, Kaohsiung 80424, Taiwan
[b] Interdisciplinary Research Center for Hydrogen Technologies and Carbon Management (IRC-HTCM), King Fahd University of Petroleum & Minerals, Dhahran 31261, Saudi Arabia
[c] Center for Theoretical and Computational Physics, National Sun Yat-sen University, Kaohsiung 80424, Taiwan

HIGHLIGHTS

- Donor-acceptor–acceptor polymers were applied for photocatalytic hydrogen evolution.
- The photocatalytic efficiency depends on the molar ratio of donor to acceptor.
- PyTzTzSO-1 achieved an outstanding HER of 32.75 mmol h^{-1} g^{-1} under UV–vis light.
- PyTzTzSO-1 realized a supreme AQY of 51.31 % at 420 nm.

GRAPHICAL ABSTRACT

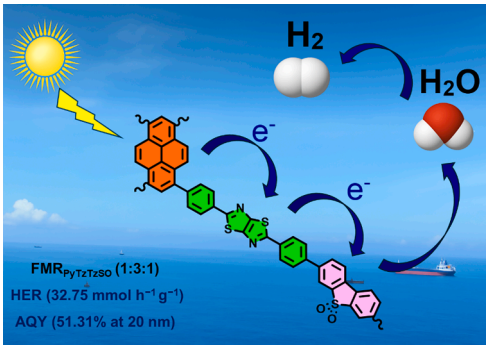

ARTICLE INFO

Keywords:
Conjugated microporous polymers
Donor-acceptor–acceptor
Thiazolo[5,4-*d*]thiazole
Statistical polymerization
Photocatalysis
Hydrogen evolution

ABSTRACT

Significant progress has recently been made in the design and preparation of conjugated microporous polymers (CMPs) as photocatalysts for hydrogen generation. However, a major challenge remains in developing CMP-based photocatalysts with enhanced photoconversion efficiency. In addition, the fixed chemical composition of the donor–acceptor (D–A) polymers' photocatalysts prohibited their efficiency. Here, a set of D-A1-A2 type polymeric photocatalysts has been statistically copolymerized by adopting pyrene (Py), thiazolo[5,4-*d*]thiazole (TzTz), and dibenzothiophene-S,S-dioxide (SO) as the D, A1, and A2, respectively, with the SO monomer possessing the higher electron-accepting capacity. Besides photocatalytic characterizations, the influence of D-to-A molar ratios on their efficiency has been studied. The obtained analyses represented that the energy gap of D-A1-A2 CMPs can be adjusted by statistical copolymerization, and the optimized photocatalyst PyTzTzSO-1 with a molar ratio of 1.0:3.0:1.0 achieved an attractive hydrogen evolution rate (HER) of 39.11 mmol h^{-1} g^{-1} under UV-visible light and of 38.61 mmol h^{-1} g^{-1} under visible light in the presence of 1 wt% of platinum (Pt)

* Corresponding author.
E-mail address: ahmedelmahdy@mail.nsysu.edu.tw (A.F.M. EL-Mahdy).
[1] Ahmed F. Saber and Huei-Ting Liao contributed equally to work and should be considered co-first authors.

https://doi.org/10.1016/j.jcis.2025.138156
Received 10 March 2025; Received in revised form 23 May 2025; Accepted 8 June 2025
Available online 9 June 2025

cocatalyst. Remarkably, the apparent quantum yield (AQY) at 420 nm stands at 51.18 %, representing the state-of-the-art for organic polymeric photocatalysts. The best photocatalytic efficiency of the PyTzTzSO-1 polymer was primarily due to its higher Brunauer–Emmett–Teller (BET) surface area, enhanced hydrophilicity, broader energy gap, as well as decreased recombination rate of photo-induced holes and electrons. Consequently, the structural design of D-A1-A2 CMPs photocatalysts with tuned components had great potential for improving photocatalytic hydrogen generation.

1. Introduction

Over the past decades, the cost of low-carbon electricity has dropped significantly, driven by substantial advancements in photovoltaics and wind energy technologies. As a result, generating renewable electricity has become more accessible and economically viable compared to constructing new fossil fuel-based power stations [1]. However, global energy consumption is still predominantly reliant on fuels rather than electricity, and low-emission fuel alternatives continue to lag behind the progress made in clean electricity generation. Due to its zero-carbon emissions and high energy density, hydrogen (H_2) is considered one of the most promising alternative energy carriers for the 21st century [2,3]. Compared to H_2 production via steam reforming, photocatalytic hydrogen evolution (PHE) through water splitting offers a more efficient and environmentally friendly approach to generating green and sustainable hydrogen energy [4–6]. However, the overall photocatalytic performance remains limited by the lack of highly efficient photocatalysts and the inherently slow kinetics of the oxygen evolution reaction [7,8]. Undoubtedly, the rational design of semiconductor photocatalysts plays a pivotal role in achieving effective H_2 evolution from water [9–12]. Inorganic semiconductor photocatalysts have been extensively designed, synthesized, and studied, and remarkable results have been accomplished [13–15]. However, their practical application in H_2 production is still challenged by several limitations, including restricted activity under ultraviolet light, limited tunability of the energy bandgap, and rapid electron–hole recombination [16,17]. Currently, polymeric photocatalysts offer several advantages, such as ease of preparation, straightforward structural modification, low cost, enhanced safety, and tunable electronic properties [18–22]. As a result, the development of organic photocatalysts has attracted growing global interest from the scientific community.

Conjugated microporous polymers (CMPs) were a subclass of organic polymeric semiconductors with π-conjugation structure [23,24] and have been applied in various applications such as gas uptake, photocatalysis, dye adsorption, sensors, transistors, and supercapacitor electrodes [25–34]. Besides, CMPs were shown to be promising photocatalysts for water splitting, possibly due to their large surface area [35,36], defined chemical structure, [37–39] excellent physicochemical and thermal stability [40], broad absorption range [41,42], and adjustable electronic and optical properties [43]. During the photocatalysis process, charge isolation and migration could be largely hindered owing to the poor dielectric constant characteristics of polymeric photocatalysts, thereby manipulating photocatalytic activity. Consequently, the engineering donor–acceptor (D-A) system within polymer structure has been confirmed as a reliable strategy for facile charge separation and transportation [44–49]. However, nearly the whole D-A polymeric photocatalysts generally prohibit the preparation using two functional monomers with equal molar ratio, so it is sophisticated to study the influence of chemical structure on the energy gap, microstructure, and photocatalytic efficiency as well [50,51].

To further improve the D-to-A molecular ratio in D-A polymeric photocatalysts, two efficient protocols for building D-π-A and D-A-A types were suggested to tune their efficiency via ternary statistical copolymerization [52,53]. For instance, Jiang's group showed an excellent hydrogen evolution rate (HER) with a value of 105 mmol h^{-1} g^{-1} through benzene unit insertion between the dibenzothiophene-S,S-dioxide acceptor (SO) and pyrene donor (Py) in D-π-A system CMPs [54], and a further enhancement of the photocatalytic performance was achieved using thiophene unit instead of benzene building block as π-bridge between Py donor and SO acceptor to expand the spectral region [53]. Also, a series of D-A-A polymeric photocatalysts with optimized molar ratio of Py and SO monomers have been synthesized by Pan's team through ternary statistical copolymerization with excellent HER value (23.3 mmol h^{-1} g^{-1}), which was two times greater than that of its corresponding D-A CMPs [52]. Additionally, the Jiang group constructed a set of D-A-A CMPs with dibenzo[*g,p*]chrysene donor and SO acceptor, which showed an outstanding HER of 214.43 mmol h^{-1} $g^{-1,}$ which was achieved with a D-to-A molar ratio of 1.0:3.0 [55].

A rational election of D and A monomers is crucial for developing organic polymers for photocatalysis and optoelectronic applications [56,57]. Py monomer was shown to serve as a polycyclic aromatic unit, which can be stacked easily through π-π interaction, leading to a great conjugation length. So, Py-based CMPs were extensively studied in the field of photocatalysis with remarkable HER values [17,58]. SO monomer with robust composition and electron-withdrawing capability is an efficient organic monomer for photocatalysis applications [59,60]. In addition, SO-based polymeric photocatalysts represent a high potential for solar-to-hydrogen conversion because of their great hydrophilicity which gives rise to better charge isolation and smaller water contact angles. Moreover, thiazolo[5,4-*d*]thiazole (TzTz) is a heterocyclic unit containing N and S atoms, which is considered an *n*-type semiconductor with high electron mobility. The insertion of TzTz unit into conjugated polymeric systems can greatly enhance the photocatalytic performance because of its planar rigidity, excellent oxidative stability, photoabsorbing ability, and electron deficiency [61,62].

According to the above discussion, in this work, three D-A1-A2 polymers (Scheme 1), in which 1,3,6,8-tetrabromopyrene (Py-4Br, Scheme S1 and Fig. S1) serves as D, 3,7-dibromodibenzo[*b,d*]thiophene 5,5-dioxide (SO-2Br, Scheme S2 and Figs. S2–S3) as a primary acceptor (A2) and 2,5-bis(4-(4,4,5,5-tetramethyl-1,3,2-dioxaborolan-2-yl) phenyl)-3a,6a-dihydrothiazolo[5,4-*d*]thiazole (TzTz-2BO, Scheme S3 and Figs. S4–S6) as the secondary acceptor (A1), were effectively polymerized via the Suzuki coupling. The as-synthesized polymers act as photo-induced electron-carrier photocatalysts for high-performance H_2 evolution. Moreover, a simple statistical copolymerization was carried out to tune the polymers' energy gap (*Eg*) to attain the "Goldilocks Zone" [63], at which better visible light harvesting and a large molecular dipole were able to improve the charge mobility and restrict the charge recombination. As a result, the PyTzTzSO-1 terpolymer had the optimal *Eg* (2.43 eV), effective electron/hole separation, and inhibited charge recombination, achieving an outstanding HER up to 32.75 mmol h^{-1} g^{-1}, outperforming other porous organic polymers. These results demonstrate that the D-A1-A2 polymeric materials have a great prospect for photocatalysis applications.

2. Experimental part

2.1. Materials and characterizations

All used solvents and chemical reagents have been obtained from commercial supplies. Potassium acetate (KOAc, ≥99.0 %), sodium bicarbonate ($NaHCO_3$, ≥99.0 %), cyclohexanone (≥99.0 %), *n*-hexane (≥99.0 %), bis(pinacolato)diboron (99.0 %), 1,1′-bis[(*diphenylphosphino*)*ferrocene*]dichloropalladium (II) (98.0 %), dibenzo[*b,d*]

thiophene-*S*,*S*-dioxide (SO, 97.0 %), and dithiooxamide (TT, 97.0 %), ascorbic acid (AA, 99.0 %), triethanolamine (TEOA, ≥99.0 %), and triethylamine (TEA, ≥99.5 %) have been purchased from Sigma–Aldrich. Tetrakis(triphenylphosphine)palladium (0) ($Pd(PPh_3)_4$, 99.0 %), and pyrene (Py, 98.0 %) have been obtained from Acros. Tetrahydrofuran (THF, ≥99.0 %), N,N-dimethylformamide (DMF, ≥99.8 %), nitrobenzene (99.0 %), chlorobenzene (≥99.5 %), dioxane (99.0 %), and dichloromethane (DCM, 99.5 %) have been obtained from J. T. Baker. *N*-bromosuccinimide (NBS, 99.0 %), bromine (Br_2, 99.5 %), 4-bromobenzaldehyde (≥98.0 %), potassium carbonate (K_2CO_3, 99.0 %), magnesium sulfate ($MgSO_4$, 99.5 %), sodium sulfate (Na_2SO_4, 99.99 %), acetone (≥99.5 %), methanol (MeOH, 99.9 %), and ethanol (EtOH, 99.5 %) have been purchased from Alfa Aesar. Sulfuric acid (H_2SO_4, 98.0 %) has been purchased from UNI-ONWARD CORP. All the characterization details of the synthesized polymers were included in the Supporting Information (SI).

2.2. Synthesis of polymeric photocatalysts

All the conjugated polymers underwent synthesis via the classical Suzuki–Miyaura coupling polymerization [14,64].

2.2.1. Synthesis of PyTzTzSO-1 CMP

Py-4Br (0.097 mmol, 50 mg, Scheme S1), SO-2Br (0.097 mmol, 36.12 mg, Scheme S2), TzTz-2BO (0.29 mmol, 158.25 mg, Scheme S3), K_2CO_3 (0.29 mmol, 40 mg) and $Pd(PPh_3)_4$ (0.005 mmol, 5.58 mg) were evacuated for 15 min before adding anhydrous DMF and H_2O (5:1, v/v; 12 mL). The reaction mixture was degassed through three freeze–pump–thaw cycles and then heated to 150 °C with stirring for 3 days. After cooling to the ambient temperature, the resulting precipitate was collected by filtration. Subsequently, the obtained CMP was washed several times with water, MeOH, and THF, respectively. Finally, the polymer was purified through Soxhlet extraction with MeOH and hexane over 2 days before drying at 100 °C to give an insoluble powder (yield: 78.23 %).

2.2.2. Synthesis of PyTzTzSO-2 CMP

Py-4Br (0.058 mmol, 30 mg, Scheme S1), SO-2Br (0.17 mmol, 65 mg, Scheme S2), TzTz-2BO (0.29 mmol, 158.25 mg, Scheme S3), K_2CO_3 (0.17 mmol, 24 mg) and $Pd(PPh_3)_4$ (0.003 mmol, 3.35 mg) were evacuated for 15 min before adding anhydrous DMF and H_2O (5:1, v/v; 12 mL). The reaction mixture was degassed through three freeze–pump–thaw cycles and then heated to 150 °C with stirring for 3 days. After cooling to the ambient temperature, the resulting precipitate was collected by filtration. Subsequently, the obtained CMP was washed several times with water, MeOH, and THF, respectively. Finally, the polymer was purified through Soxhlet extraction with MeOH and hexane over 2 days before drying at 100 °C to give an insoluble powder (yield: 83.35 %).

2.2.3. Synthesis of PyTzTzSO-3 CMP

Py-4Br (0.048 mmol, 25 mg, Scheme S1), SO-2Br (0.19 mmol, 72.23 mg, Scheme S2), TzTz-2BO (0.29 mmol, 158.25 mg, Scheme S3), K_2CO_3 (0.14 mmol, 20 mg) and $Pd(PPh_3)_4$ (0.002 mmol, 2.79 mg) were evacuated for 15 min before adding anhydrous DMF and H_2O (5:1, v/v; 12 mL). The reaction mixture was degassed through three freeze–pump–thaw cycles and then heated to 150 °C with stirring for 3 days. After cooling to the ambient temperature, the resulting precipitate was collected by filtration. Subsequently, the obtained CMP was washed several times with water, MeOH, and THF, respectively. Finally, the polymer was purified through Soxhlet extraction with MeOH and hexane over 2 days before drying at 100 °C to give an insoluble powder (yield: 85.66 %).

3. Results and discussion

3.1. Molecular design and preparation

To enhance the efficiency of Frenkel exciton isolation in D-A CMPs, mitigate the electron-hole recombination, and, thereby, photocatalytically generate H_2 from water, an innovative proposal has been suggested that involves the development of a series of CMPs with a D-A1-A2 ternary system, characterized by a considerable dipole moment. As depicted in Scheme 1, the desired D-A1-A2 polymers have been constructed using a statistical copolymerization protocol. This approach enables systematic structural control of the synthesized CMPs and the adjustment of their dipole moment through various monomer feed molar ratios (FMR) [14,65]. The tunability of FMR serves as a variable to

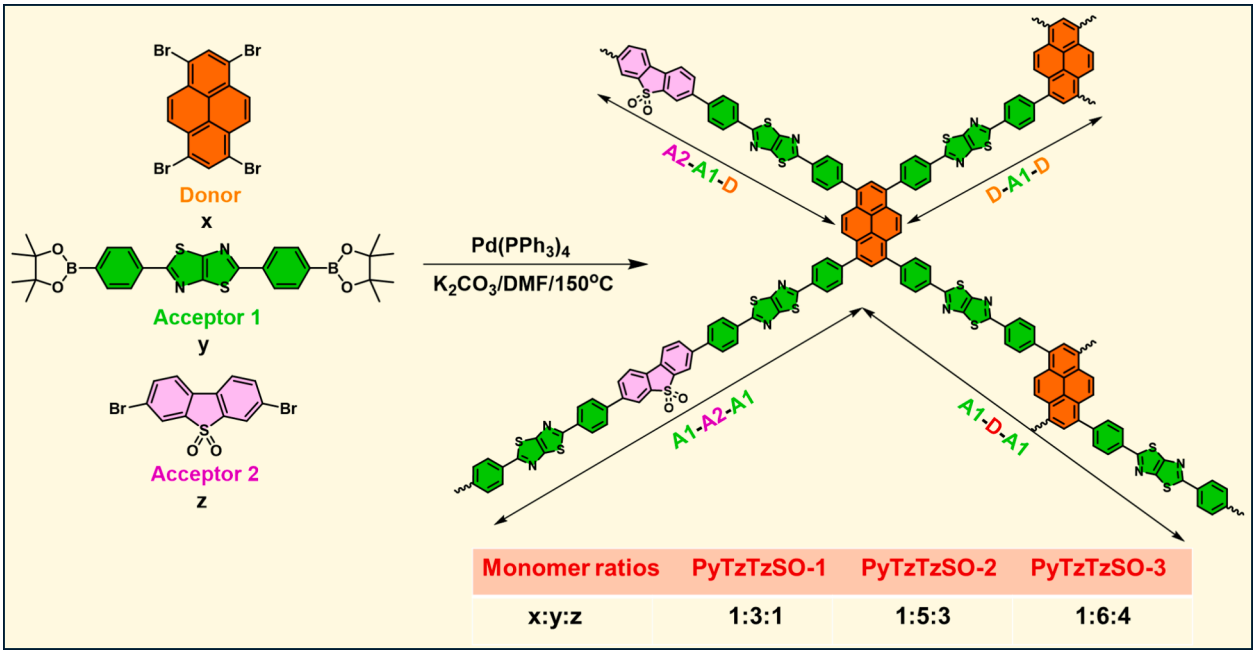

Scheme 1. Synthetic strategy of D-A1-A2 type photocatalysts.

adjust the electronic composition of polymers, aiming to achieve an optimized D-A1-A2 structure for enhanced photocatalytic H_2 evolution. The resulting D-A1-A2 polymers are denoted as PyTzTzSO-1, PyTzTzSO-2, and PyTzTzSO-3 with corresponding monomer FMR of 1.0:3.0:1.0, 1.0:5.0:3.0, and 1.0:6.0:4.0, respectively. The polymerization reactions were conducted using the traditional catalytic Suzuki coupling polycondensation, and the complete procedures have been provided in the experimental part.

3.2. Structural characterizations

The utilized monomers Py-4Br, TzTz-2BO, and SO-2Br have been synthesized following procedures described in the literature [43,44,48]. The chemical structure of the obtained CMPs is specifically characterized by the Fourier transform infrared spectroscopy (FTIR), solid-state ^{13}C nuclear magnetic resonance (NMR) spectra, and X-ray photoelectron spectroscopy (XPS). The FTIR profile of our polymers' photocatalysts did not exhibit absorption bands at 2984, 2927, and 1363 cm^{-1}, which were characteristic of the aliphatic C—H and B–O vibrations of TzTz-2BO. Besides that, no distinct C–Br absorption bands were observed close to 675 and 702 cm^{-1} for the respective Py-4Br and SO-2Br monomers. Furthermore, absorption bands were indeed observed at 3025, 3029, and 3026 cm^{-1}, featuring aromatic C—H, and absorption bands at (1307, 1157 cm^{-1}), (1308, 1160 cm^{-1}) and (1308, 1160 cm^{-1}) indicative of O═S═O functional group, as well as sharp absorption bands at 1604, 1593 and 1593 cm^{-1} corresponding to the C═C stretching vibrations for PyTzTzSO-1, PyTzTzSO-2 and PyTzTzSO-3, respectively (Figs. S7–S9 and Fig. 1A).

The solid-state ^{13}C NMR spectra provided additional proof of the complete condensation between monomers, as no absorption peaks were noticed for pinacolato carbons. Instead, broad absorption signals were evident, however, for the phenyl carbons of the PyTzTzSO-1, PyTzTzSO-2, and PyTzTzSO-3 CMPs, spanning the ranges 120–142, 117–143, and 122–144 ppm, respectively. Weak signals were also observed for the N-C═C-N carbon nuclei and the C-SO_2 carbon at 148–153 ppm for PyTzTzSO-1, at 149–154 ppm for PyTzTzSO-2, and at 150–154 ppm for PyTzTzSO-3. Furthermore, wide peaks were noticed in the range of 161–170 ppm for PyTzTzSO-1, 165–171 ppm for PyTzTzSO-2, and 166–172 ppm for PyTzTzSO-3, which were related to the N═C–S carbons (Fig. 1B).

Moreover, XPS measurements were conducted to thoroughly investigate the chemical composition and surface chemical states of the synthesized polymers. As illustrated in the XPS spectroscopy (Fig. 2a), the predominant chemical constituents of PyTzTzSO-1, PyTzTzSO-2, and PyTzTzSO-3 were carbon (C), nitrogen (N), oxygen (O), and sulfur (S), indicating the presence of pyrene, thiazolyl, and sulfone functionalities within all samples. The high-resolution XPS analyses of C 1s show the binding energy of polymers at 285.32 eV, N 1s at 399.88 eV, O 1s at 532.71 eV, S 2s at 228.11 eV, and S 2p at 164.8 eV. To examine the nature of carbon atoms in our polymer materials, fitting analyses have been applied, in which the C1s signal exhibited three distinct peaks located around 283.95–283.80 eV, 284.05–284.02 eV, and 284.55–284.42 eV, indicative of C—S, C—N, and C═C functional groups, respectively, for the three polymers. In addition, the binding energies of the sp^2-N of D-A1-A2 polymers were found to be 398.34, 398.36, and 398.39 eV for PyTzTzSO-1, PyTzTzSO-2, and PyTzTzSO-3, respectively. Furthermore, the O1s peak fitting resulted in a major peak centered at 531.65 eV, 531.63 eV, and 531.69 eV, which were related to the S═O group of PyTzTzSO-1, PyTzTzSO-2, and PyTzTzSO-3, respectively. The S species in SO-based polymers have been located at 163.67 and 164.71 eV for PyTzTzSO-1, at 163.59 and 164.67 eV for PyTzTzSO-2, and at 163.61 and 164.71 eV for PyTzTzSO-3, which were attributed to the S $2p_{1/2}$ and S $2p_{3/2}$ in the S═O functionality, respectively (Fig. S10 and Table S1) [66,67]. Powder X-ray diffraction (XRD) profiles of the studied CMPs exhibited no discernible diffraction peaks, suggesting the amorphous nature of all polymers (Fig. 2b), consistent with findings from other reported CMPs [68,69].

A prominent characteristic of these polymers lies in their rigidity and substantial crosslinking, leading to a notable decrease in solubility in various solvents and an enhancement in thermal stability. For feasible applications of our synthesized polymeric materials, their thermal stability, which is a significant property of porous materials, has been investigated. The thermogravimetric analysis (TGA) curves of D-A1-A2 polymers are shown in Fig. S11 and Table S2. Weight loss can be divided into three main stages in the testing process. A small weight loss takes place before 150 °C, which is caused by the vaporization of low-boiling solvents and water molecules that are trapped in the CMP pores. Whereas the larger weight loss occurs at the second stage between 500 and 600 °C, owing to the thermal decomposition of some oligomers. The final stage for weight loss happens after 600 °C, corresponding to the carbonization process. The analysis curves showed that our prepared CMPs possessed significant thermal stabilities, in which PyTzTzSO-1, PyTzTzSO-2, and PyTzTzSO-3 polymers exhibited close values of 10 % mass loss (T_{d10}) at 555, 557, and 532 °C, respectively. Even at higher temperatures (800 °C), there is still more than 60 % weight retention, with char yield values of 67 %, 66 %, and 64 % corresponding to PyTzTzSO-1, PyTzTzSO-2, and PyTzTzSO-3 CMPs, respectively, which proves their high thermal stabilities.

3.3. Porosity and morphological characterization

N_2 sorption isotherms and pore size distributions (PSDs)

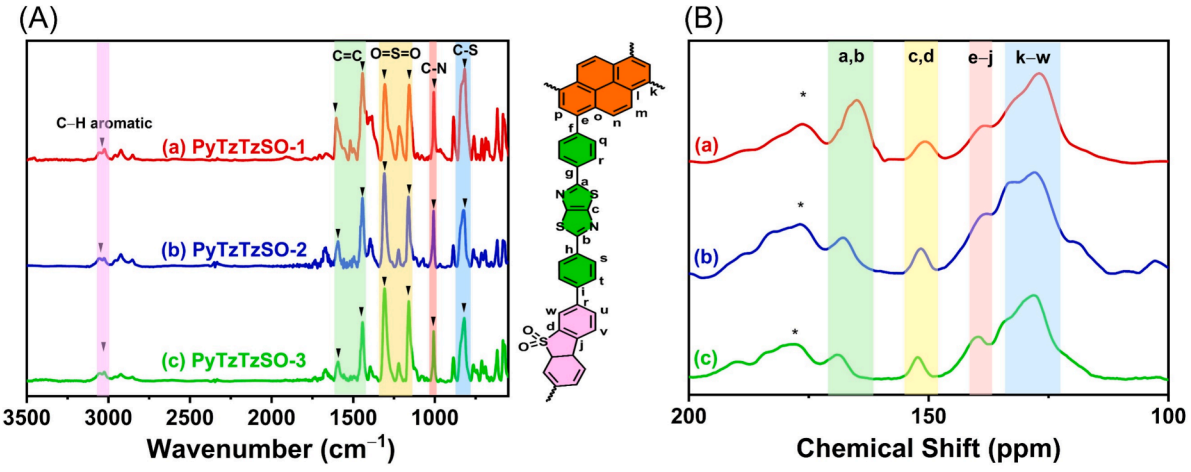

Fig. 1. (A) FTIR spectroscopic analysis and (B) solid state ^{13}C NMR spectra of (a) PyTzTzSO-1, (b) PyTzTzSO-2, and (c) PyTzTzSO-3 polymeric materials.

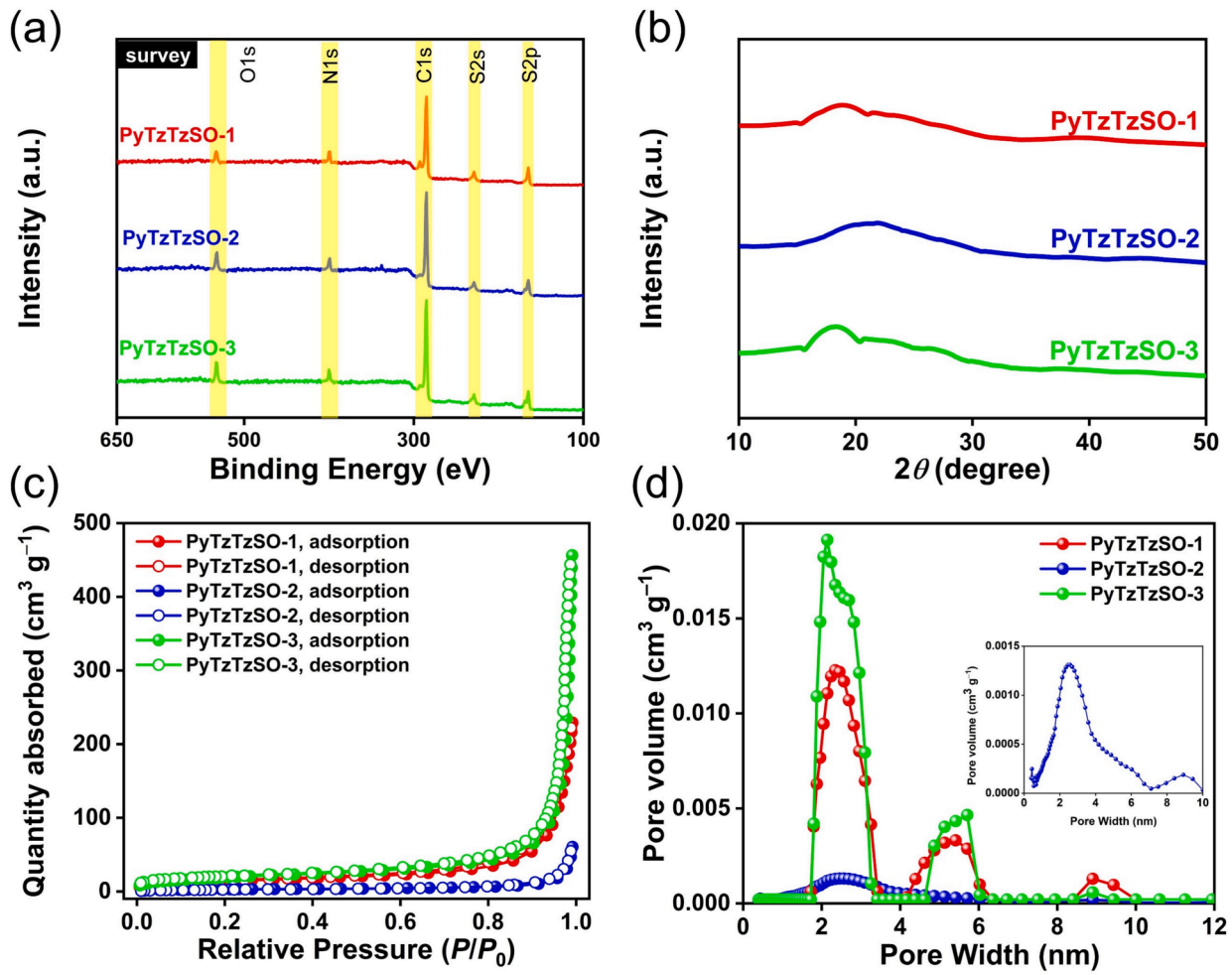

Fig. 2. (a) XPS spectra, (b) XRD profiles, (c) N_2 adsorption/desorption isotherms, and (d) pore size distribution curves of the PyTzTzSO-1, PyTzTzSO-2, and PyTzTzSO-3 CMPs.

demonstrated that all the CMPs under investigation exhibited porosity with a microporous nature. This is substantiated by the sharp ascent in the N_2 isotherms at lower relative pressures and consistent PSDs with a micropore diameter of around 1.0 nm (Fig. 2c,d, and Table 1). The specific surface areas, determined by Brunauer-Emmett-Teller (BET) analysis, for PyTzTzSO-1, PyTzTzSO-2, and PyTzTzSO-3 are 251, 100, and 169 $m^2 g^{-1}$, respectively. As indicated by the test results, there is an observed decrease and then an increase in the specific surface area with the rising SO and TzTz monomer contents from PyTzTzSO-1 to PyTzTzSO-3. The variation in BET values among the polymers might be attributed to differences in monomer structures and alterations in their FMR. Furthermore, the produced D-A1-A2 CMPs indeed showed broad PSDs, with estimated pore diameters and pore volumes at 1.65–3.59/4.17–6.36/8.40–10.00 nm and 0.34 $cm^3 g^{-1}$ for PyTzTzSO-1, 0.73–6.71/7.50–10.00 nm and 0.08 $cm^3 g^{-1}$ for PyTzTzSO-2, and 1.72–3.42/4.62–6.02 nm and 0.68 $cm^3 g^{-1}$ for PyTzTzSO-3, respectively. These wide PSDs observed in our prepared polymers could be attributed to interparticle cavities within CMP frameworks, as reported in the literature [70]. As depicted above, the chosen Py-4Br donor, with four polymerizable sites, establishes 3D cross-linked polymeric frameworks characterized by large specific surface areas. Additionally, by adjusting the feed ratio of comonomers, it is possible to conveniently obtain polymeric materials with great BET surface areas, subsidiary to an efficient photocatalysis process [67]. In statistical polymerization of terpolymers, different pore sizes often emerge due to several interrelated factors stemming from the random incorporation of multiple monomers with differing shapes, sizes, and reactivities. Therefore, the random sequence of monomers interrupts periodic packing, producing both micropores and mesopores. Also, monomers with different sizes or geometries (e.g., planar vs. twisted, linear vs. bulky) disrupt uniform packing, which causes incomplete or uneven cross-linking, leaving voids of varied dimensions. For instance, a bulky monomer may prevent close packing, creating larger pores, while smaller, planar monomers can form tight micropores. Additionally, the FMR and reactivity of the monomers influenced how densely the polymer chains are crosslinked, in which areas with high crosslinking may result in smaller pores, while low crosslinking zones leave larger voids. Moreover, the rapid formation of covalent bonds can lock-in local structure before the system reaches equilibrium, which results in amorphous regions with irregular pore morphology [71–73]. Therefore, in the case of the PyTzTzSO-1, PyTzTzSO-2, and PyTzTzSO-3 terpolymer systems, the emergence of different pore sizes is consistent with the stochastic spatial arrangement of monomers with distinct functionalities

Table 1
BET parameters of the synthesized polymers.

CMPs	S_{BET} ($m^2 g^{-1}$)	Pore size (nm)	Pore volume ($cm^3 g^{-1}$)
PyTzTzSO-1	251	1.6–3.6/4.1–6.3/8.4–10.0	0.34
PyTzTzSO-2	100	0.7–6.7/7.5–10.0	0.08
PyTzTzSO-3	169	1.7–3.4/4.6–6.0	0.68

and geometries. The observed bimodal PSD—centered around ~3 nm and ~6 nm—can be rationalized by the diverse connectivity motifs illustrated in Scheme 1. Shorter sequence such as D–A1–D is likely result in more compact network segments that correlate with micropores (~3 nm), while more extended or branched linkages, such as D–A1–A2–A1 or D–A1–A2, introduce greater free volume and less efficient packing, contributing to the formation of larger mesopores (~6 nm).

The morphological structures of the resulting porous polymers were analyzed through scanning electron microscopy (SEM) and transmission electron microscopy (TEM). Based on SEM images, it is observed that all examined CMPs exhibit small agglomerated spherical shapes, displaying a similar nanoparticle morphology (Fig. 3a–c). Additionally, the elemental mapping conducted via energy-dispersive X-ray spectroscopy (EDS) represented a homogeneous distribution of C, N, O, and S atoms across polymer skeletons (Fig. S12). Moreover, the porous structures of the synthesized D-A1-A2 CMPs were further validated through TEM imaging. The formation of this porous structure can be attributed to the highly cross-linked frameworks of the synthesized CMPs. Circular-shaped nanoparticles have been identified, featuring internal diameters within a specific range (100–600 nm), and showing amorphous texture (Fig. 3d–f). The elemental analyses of the as-prepared polymers have been investigated using EDS spectroscopy (Fig. S13). The EDS pattern of the PyTzTzSO-1 polymer exhibited four peaks at 0.009, 0.034, 0.271, and 2.319 KeV, representing C, N, O, and S atoms, respectively. The corresponding values for the PyTzTzSO-2 polymer were observed to be 0.259, 0.317, 0.511, and 2.305 KeV, respectively. Whereas the obtained signals for PyTzTzSO-3 polymer were found to be 0.259, 0.317, 0.521, and 2.305 KeV, respectively.

We measured the water contact angle (CA) for the obtained copolymers to evaluate their hydrophilic nature. The results indicated an observed decrease in CA from 83.4° for PyTzTzSO-3, 59.6° for PyTzTzSO-2, to 53.5° for PyTzTzSO-1, illustrating a stepwise improvement in hydrophilicity from PyTzTzSO-3 to PyTzTzSO-1 (Fig. S14). The high hydrophilicity, characterized by a small CA of water, facilitates direct contact between the reaction solution and the surface of polymers, thereby enhancing photocatalytic performance [74].

3.4. Optical efficiency and HOMO–LUMO energy gap

Investigation of the visible-light absorption characteristics for our polymers under study was conducted using ultraviolet/visible (UV/vis) absorption spectroscopy. From the obtained Tauc plot, the Eg of conjugated polymers have been calculated, whereas cyclic voltammetry (CV) plots have been utilized to determine the lowest unoccupied molecular orbital (LUMO) values. (Fig. S15) As observed in the UV/vis absorption curves (Fig. 4a), our synthesized CMPs demonstrate a wide visible-light absorption domain (400–800 nm). In comparison to classical D-A CMPs, D-A1-A2 type polymers with higher intramolecular charge transfer (ICT) from D to A1 to A2 show a broader range of visible light response with a dark color (Fig. S16). Interestingly, with increasing SO and TzTz contents, the polymers exhibited a bathochromic shift. Additionally, the insertion of the SO group modulates the Eg of the resulting polymers within a range of 2.43 to 2.55 eV (Fig. 4b and c). Notably, the prepared terpolymer PyTzTzSO-1 exhibits a narrow Eg value of 2.43 eV and the broadest visible light absorption domain. In general, a broader light response domain suggests an extended π-conjugated chain, leading to improved electron delocalization, which is advantageous for photocatalytic reactions [74].

3.5. Electron transport dynamics

Photo-electrochemical measurements were conducted to observe the suppression of backward charge recombination and the enhancement of forward charge isolation characteristics, as critical variables influencing the photocatalytic performance of polymeric materials. Photoluminescence (PL) spectra, arising from the combination of photogenerated electrons and holes, serve as a reliable method for characterizing the rate of charge recombination. As depicted in Fig. 4d, the produced polymers revealed various emission peaks and intensities. The PyTzTzSO-3 terpolymer possessed the smallest PL intensity, demonstrating that its charges/holes recombination was greatly suppressed compared to other CMPs; this was mainly due to the extended π-conjugation and considerable energy level gradient. The intensities of the resulting PL peaks have been inclined in the order PyTzTzSO-3 < PyTzTzSO-2 < PyTzTzSO-1. However, this trend didn't agree with the actual order of their photocatalytic performance, in which PyTzTzSO-1

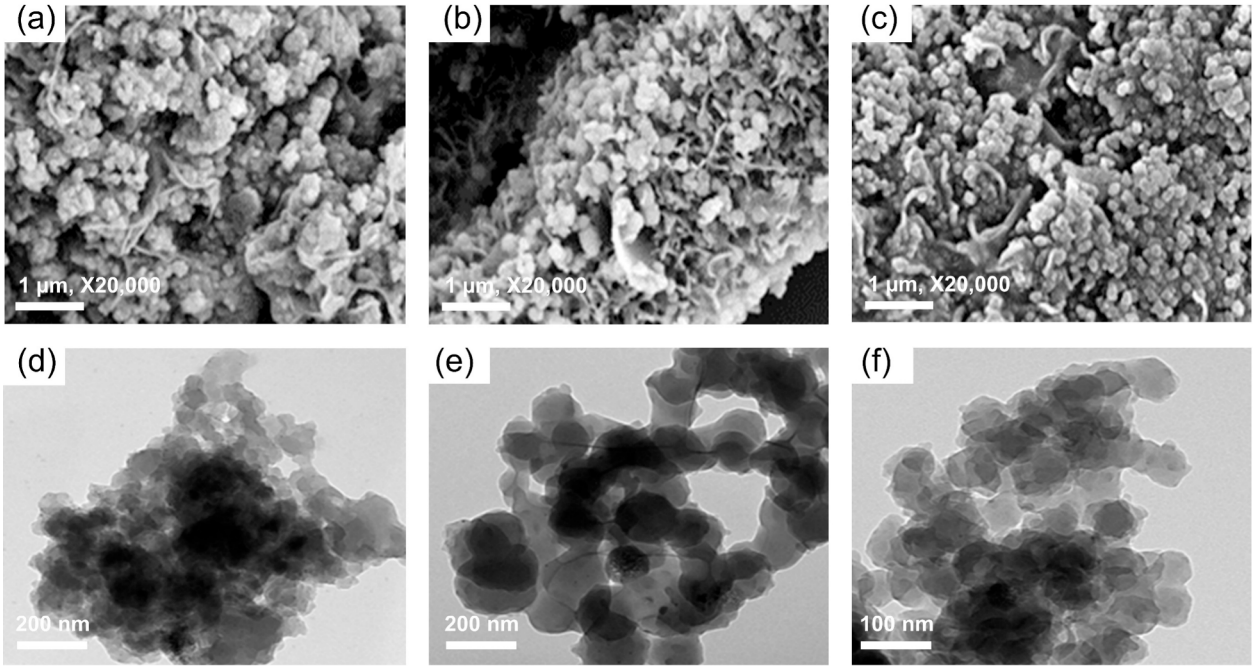

Fig. 3. FE-SEM photos of (a) PyTzTzSO-1, (b) PyTzTzSO-2, and (c) PyTzTzSO-3 CMPs. TEM photos of (d) PyTzTzSO-1, (e) PyTzTzSO-2, and (f) PyTzTzSO-3 CMPs.

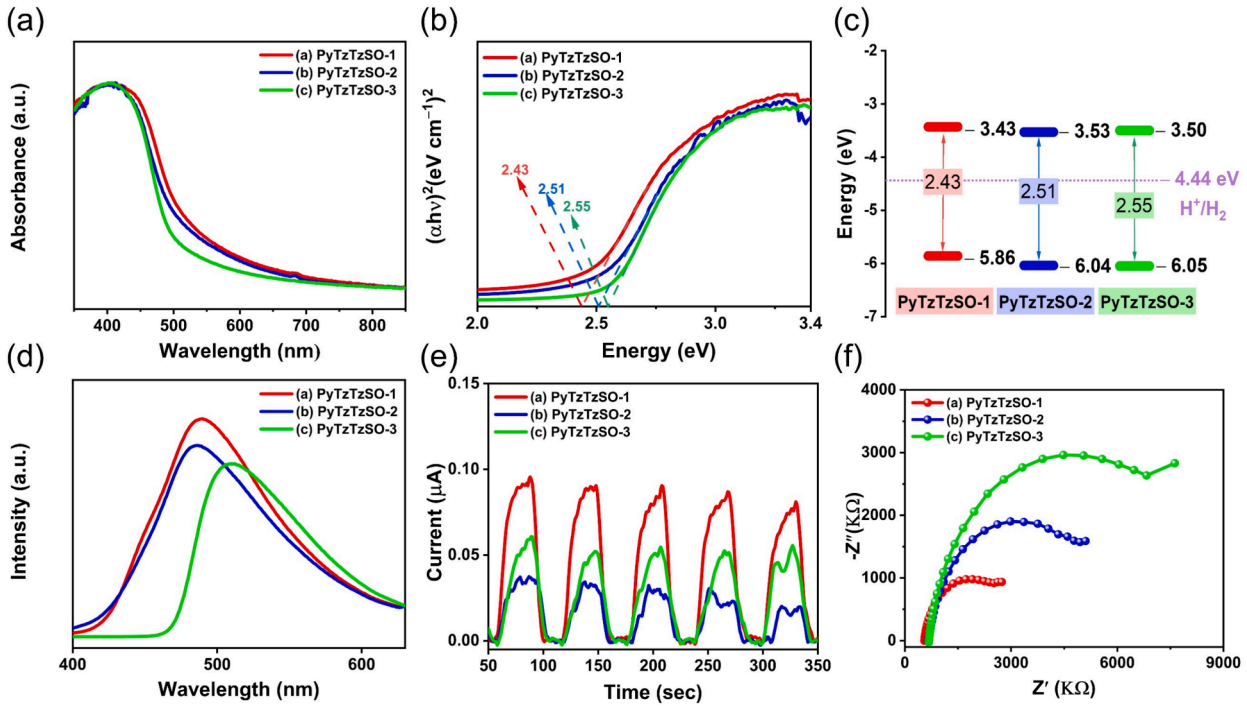

Fig. 4. (a) UV–vis diffuse absorption spectra, (b) Tauc plots (from UV–visible spectra), (c) electronic band structures, (d) PL spectra, (e) transient photocurrent measurements, and (f) Nyquist plots, of all D-A1-A2 polymers.

exhibited the top photocatalytic efficacy. This behavior may be attributed to other variables such as a smaller energy gap, the highest BET surface area, and the top hydrophilicity of the PyTzTzSO-1 CMP in comparable to others. The observed, red-shifted emission of the PyTzTzSO-3 at approximately 509 nm could be related to the highest SO content with an efficient electron-withdrawing nature [14,75]. In addition, A red shift in the PL spectra of the PyTzTzSO-3 with the highest A content can be attributed to several key structural and electronic factors: The first one is that increasing the A content in the polymer chain strengthens ICT between D and A units. This leads to lower energy excitons, which emit at longer wavelengths. The second factor is that with more A units, an improvement in π-conjugation across the structure will occur. This extended conjugation delocalizes the exciton, lowering the energy of emission and causing a red shift. The third factor is that the higher A content can promote π–π stacking or aggregation, especially in amorphous CMPs. Aggregation typically results in red-shifted emission due to the formation of excimers or lower-energy aggregate states [76–78]. Furthermore, the transient photocurrent measurement of the PyTzTzSO-1 polymer was greater than those of the other polymers, suggesting the most rapid photoresponse (Fig. 4e). Meanwhile, according to electrochemical impedance spectroscopy (EIS), the PyTzTzSO-1 polymer had lower resistance than the others, confirming excellent interfacial charge transfer, consistent with the photocurrent analysis (Fig. 4f). Based on the obtained data, the building of D-A1-A2 type polymers not only enhances forward charge isolation but prohibits charge recombination as well, thereby boosting photocatalytic efficiency.

3.6. Photocatalytic experiments

The as-synthesized polymers were tested as photocatalysts for H_2 generation using a visible light source (λ = 380–780 nm) at 25 °C for a duration of 4 h. Each photocatalytic system was conducted in a glass photoreaction cell by the addition of a sacrificial electron donor (SED) to the suspended polymer in a mixture of DMF and H_2O. The released gas was observed, measured, and analyzed into a gas chromatograph (GC) every hour. To recognize a convenient SED, we evaluated solutions of AA, TEOA, and TEA by investigating the hydrogen evolution rate (HER) within a 4 h period under ultraviolet–visible light irradiation, in the absence of a platinum (Pt) cocatalyst (Figs. 5a and S17). The performance of the D-A1-A2 polymers was significantly greater in AA solution compared to the TEOA and TEA solutions. Consequently, we utilized AA at a definite pH (4.0) as the sacrificial agent in the following optimization experiments.

Fig. S18 compares the time-dependent H_2 evolution performance of PyTzTzSO-1, PyTzTzSO-2, and PyTzTzSO-3 CMPs under two different light irradiation conditions: UV–visible light and visible light only, using 1 mM AA as a sacrificial agent. Under UV–Visible irradiation, PyTzTzSO-1 exhibited the highest photocatalytic activity, reaching approximately HER of 39.11 mmol g^{-1} h^{-1}, followed by PyTzTzSO-2 (~33.44 mmol g^{-1} h^{-1}), while PyTzTzSO-3 shows minimal hydrogen evolution (~9.15 mmol g^{-1} h^{-1}). A similar trend is observed under visible light irradiation, although with slightly lower overall activity. PyTzTzSO-1 and PyTzTzSO-2 still demonstrated high HER (about 32.75 and 28.56 mmol g^{-1} h^{-1}, respectively), confirming their strong absorption in the visible region and efficient charge separation. In contrast, PyTzTzSO-3 continues to exhibit poor performance under visible light, indicating limited photoresponse and less effective charge dynamics. These results suggest that PyTzTzSO-1 and PyTzTzSO-2 are highly active and responsive under both UV–visible and visible light. For practical applications, photocatalytic reactions were carried out under visible light irradiation. We also investigated the effects of varying the weight amounts of our three D-A1-A2 CMPs (2.0, 5.0, and 10.0 mg) on their photocatalytic efficacy. We observed that the HER efficacy of polymers decreased as their mass increased, with the highest performance achieved using 2.0 mg of the catalysts (Figs. S19 and S20). This irreversible relationship between the HER and the amount of photocatalyst was likely due to reduced light transmission and less effective utilization of higher light intensities. The palladium (Pd) catalyst employed during the polymerization process has been reported to exhibit co-catalytic activity in photocatalytic H_2 evolution reactions [79]. Elevated levels of residual Pd (>0.24 wt%) remaining in polymeric photocatalysts synthesized via

Pd-catalyzed polymerization have been shown to enhance H_2 evolution performance [80]. In this study, the PyTzTzSO-1, PyTzTzSO-2, and PyTzTzSO-3 polymers contained 0.10, 0.12, and 0.11 wt% of Pd, respectively. Therefore, no clear correlation was observed between the Pd content and the photocatalytic performance of the polymers. Instead, the differences in their H_2 evolution efficiencies are primarily attributed to variations in their molecular structures rather than the residual Pd content. An efficient photocatalyst should demonstrate long-term stability and sustained performance for practical applications. Therefore, under the optimized conditions for H_2 generation, we examined the impact of varying the amounts of Pt co-catalyst (1.0, 5.0, and 10.0 wt% H_2PtCl_6). Remarkably, the inclusion of only 1 wt% of Pt in the CMP suspension led to outstanding HER under visible irradiation (Fig. S21). With the incorporation of Pt as a co-catalyst, all three polymers exhibited enhanced hydrogen production compared to their Pt-free counterparts. PyTzTzSO-1 demonstrated the highest performance, achieving approximately a HER of 38.61 mmol g^{-1} h^{-1}, followed by PyTzTzSO-2 with about 34.94 mmol g^{-1} h^{-1}. PyTzTzSO-3, while still significantly less active than the other two, showed a marked improvement, reaching around 10.93 mmol g^{-1} h^{-1} (Table 2). The enhancement in photocatalytic activity upon Pt loading is attributed to the improved charge separation and more efficient proton reduction facilitated by Pt, which serves as an electron trap and active site for hydrogen evolution. These results confirmed the beneficial role of Pt in boosting photocatalytic efficiency and further highlight PyTzTzSO-1 and PyTzTzSO-2 as promising polymer photocatalysts for solar hydrogen production. The long-term photocatalytic cycling tests demonstrated that all PyTzTzSO-1, PyTzTzSO-2, and PyTzTzSO-3 CMPs exhibited excellent durability and photostability, as manifested by their performance under continued irradiation for 20 h (Figs. 5b and S22). After 20 h of photocatalytic H_2 evolution, the photocatalyst powders PyTzTzSO-1, PyTzTzSO-2, and PyTzTzSO-3 were collected by filtration and subsequently analyzed using FTIR and FE-SEM to assess their structural and morphological stability. The FTIR spectra recorded before and after the photocatalytic process revealed that the key vibrational bands of all three materials remained at nearly the same wavenumbers, suggesting that their molecular frameworks were preserved without significant degradation (Figs. S23-25). Additionally, after completing four cycles of photocatalytic H_2 production, FE-SEM images confirmed that the overall morphology of the PyTzTzSO-based CMPs remained unchanged (Fig. S26). These results collectively demonstrate that the materials possess excellent chemical and morphological stability under prolonged photocatalytic conditions.

The control photocatalytic H_2 evolution measurements of PyTzTzSO-1, PyTzTzSO-2, and PyTzTzSO-3 CMPs under different conditions were clearly demonstrated in Figs. 5c and S27. In the presence of 1 M AA and under visible light irradiation, PyTzTzSO-1, PyTzTzSO-2, and PyTzTzSO-3 CMPs exhibited a significant increase in H_2 production. The distinct ON/OFF light switching behavior confirmed that H_2 generation is directly driven by light, highlighting the true photocatalytic nature of the process. In contrast, when AA is omitted, the H_2 evolution rate was markedly reduced, indicating that severe electron–hole recombination occurred in the absence of an efficient hole scavenger. The absence of a sacrificial reagent leads to inefficient hole removal, rapid recombination, and low H_2 evolution activity. AA plays a critical role by consuming holes rapidly, allowing electrons to accumulate and participate in proton reduction more effectively. Thus, the presence of a sacrificial agent is essential for high photocatalytic activity in CMP-based systems. Furthermore, in the control experiment without both the catalyst and AA, negligible H_2 production was observed. These results underscore the critical role of AA in suppressing charge recombination and enabling efficient proton reduction, thus demonstrating that CMP functions effectively as a photocatalyst only when paired with a sacrificial reagent. Moreover, the photocatalytic hydrogen production over time in the presence of 1 M AA without the addition of a photocatalyst was tested as shown in Fig. S28. The amount of H_2 generated remained extremely low, reaching only about 0.012 mmol g^{-1} after 4 h, with minimal incremental increases. This result confirmed that AA alone does not contribute to any significant H_2 evolution under visible light irradiation. The H_2 production observed is likely attributed to background noise or non-catalytic side reactions. Importantly, this control experiment underscores the necessity of a photocatalyst to drive the hydrogen evolution process, highlighting that AA functions solely as a sacrificial hole scavenger and not as a photoactive species. In conclusion, the PyTzTzSO-1, PyTzTzSO-2, and PyTzTzSO-3 CMPs exhibited notable HERs of 32.75, 28.56, and 4.17 mmol g^{-1} h^{-1}, respectively, under visible light irradiation without the use of a Pt co-catalyst (Fig. 5d). Upon the addition of 1 wt% Pt, their HERs under visible light increased to 38.61, 34.94, and 10.93 mmol $g^{-1}h^{-1}$, respectively, as summarized in Table 2. Furthermore, under UV–visible light irradiation without Pt, the PyTzTzSO-1, PyTzTzSO-2, and PyTzTzSO-3 CMPs achieved HERs of 39.11, 33.44, and 9.15 mmol g^{-1} h^{-1}, respectively, further confirming their intrinsic photoactivity and potential for noble-metal-free photocatalysis.

At present, polymeric photocatalysts possess lower apparent quantum yield (AQY) values. It is stated that the AQY of polymer-based photocatalysts has never been attained as great as that of modified g-C3N4 or inorganic materials, even at larger wavelengths (>420 nm). The AQYs of the polymeric photoabsorbers were measured with three different bandpass filters (420, 460, and 500 nm) for the assessment of spectral contributions to HER (Fig. S29). Based on the utilized light wavelengths (420, 450, and 600 nm), the highly efficient PyTzTzSO-1 photocatalyst had superb AQYs of 51.18 %, 16.08 %, and 3.37 % respectively, which were among the highest recorded values until now (Fig. 6). Table S3 shows the photocatalytic performance of various polymeric photocatalysts under visible-light irradiation. Notably, our polymeric candidates, with optimized photocatalytic conditions, exhibited the greatest HER.

To substantiate the superiority of the D–A1–A2 structures in

Table 2
Photophysical properties of H_2 evolution rates for all the polymers.

Polymer	HOMO/LUMO (eV)[a,b]	Bandgap (eV)[c]	HER (mmol $g^{-1}h^{-1}$)[d]	HER (mmol $g^{-1}h^{-1}$)[e]	AQY (%)[f]		
					420 nm	460 nm	500 nm
PyTzTzSO-1	−5.86/−3.43	2.43	32.75	38.61	51.31	16.08	3.37
PyTzTzSO-2	−6.04/−3.53	2.51	28.56	34.94	32.15	10.81	3.4
PyTzTzSO-3	−6.05/−3.50	2.55	4.17	10.93	5.88	1.58	0.58

[a] HOMO calculated using photoelectron spectra (mean ± 0.03, n = 3).
[b] LUMO = EHOMO – Eg.
[c] Calculated from Tauc plots.
[d] Conditions; 2 mg of polymer in 10 mL of a mixture of water/DMF (9:1)/1M AA, measured under 350-W Xe light (AM 1.5; λ = 380–780 nm; 1000 W m−2) (mean ± 2.6, n = 3).
[e] 2 mg of polymer + 1 wt% Pt in 10 mL of a mixture of water/DMF (9:1)/1M AA, measured under 350-W Xe light (AM 1.5; λ = 380–780 nm; 1000 W m−2) (mean ± 2.6, n = 3).
[f] AQYs measured at 420, 460, and 500 nm (mean ± 0.1, n = 3).

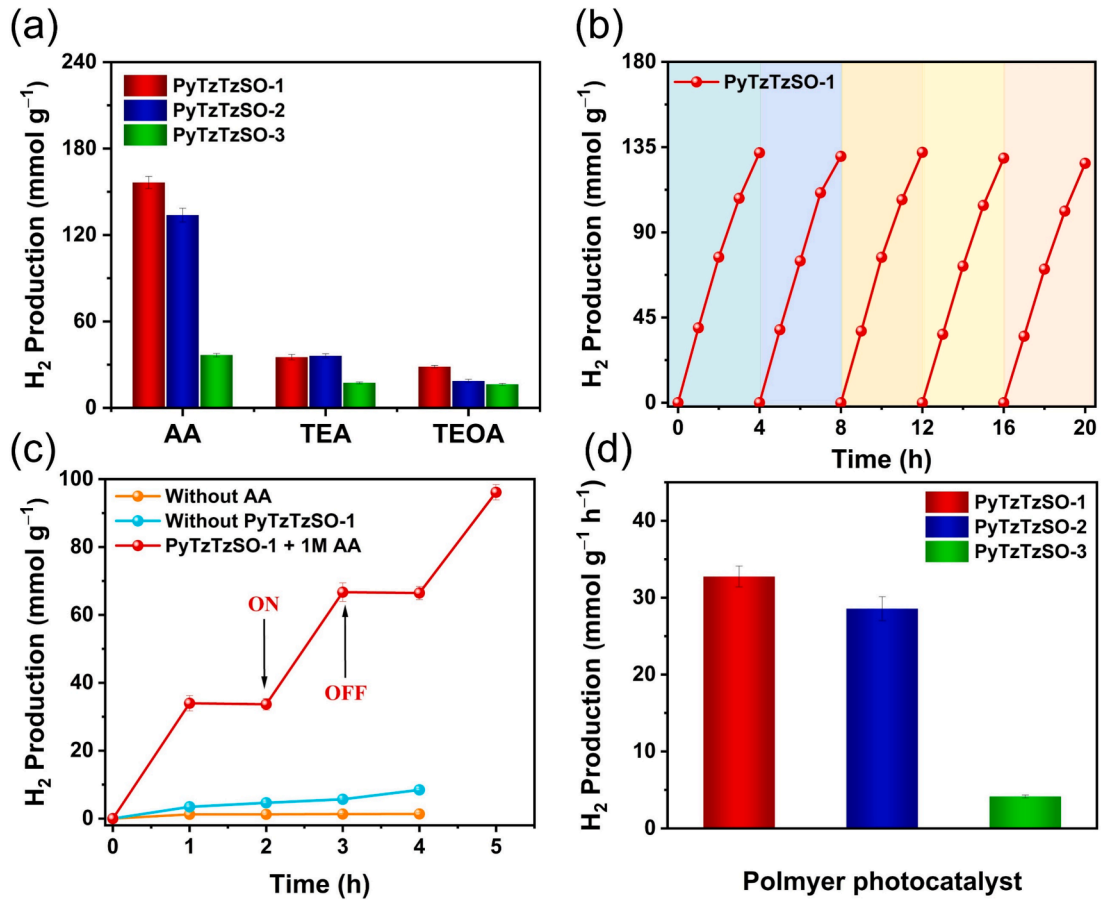

Fig. 5. (a) Effect of sacrificial agent on HER of polymers under UV–visible irradiation, (b) stability test for PyTzTzSO-1 in presence of 1 wt%Pt and under visible irradiation, (c) control experiment for PyTzTzSO-1 under visible irradiation, and (d) H_2 evolution under visible-light irradiation for the prepared polymers.

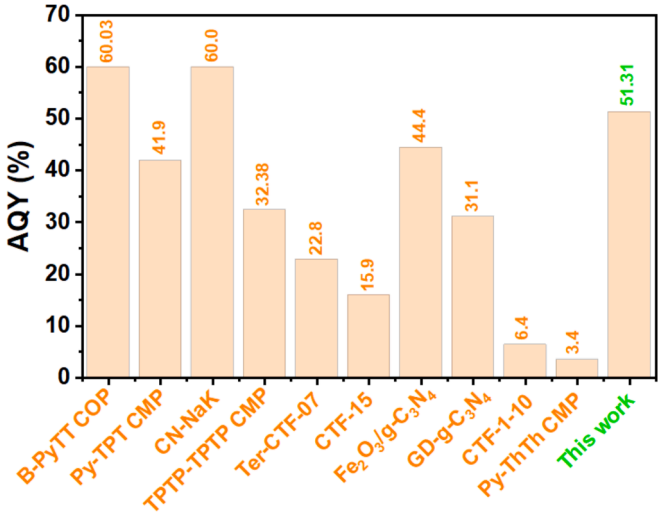

Fig. 6. Comparison of AQY of the synthesized PyTzTzSO-1 polymer at 420 nm with other reported competitive values.

photocatalytic H_2 evolution, we have evaluated the intrinsic photocatalytic activities of the individual monomers under identical reaction conditions. As shown in Fig. S30, the HERs of Py-4Br, SO-2Br, and TzTz-2BO were significantly lower than those of the corresponding D–A1–A2 polymers. Among the monomers, Py-4Br exhibited the highest HER, followed by TzTz-2BO, while SO-2Br showed minimal activity. These results confirm that while the monomers possess some inherent photoactivity, their performance is markedly inferior to that of the fully conjugated D–A1–A2 polymer networks. This demonstrates that the integration of D and dual A units within a conjugated polymer backbone significantly enhances charge separation and transfer, leading to superior photocatalytic hydrogen evolution performance.

To further validate the enhanced performance of D–A1–A2 systems, we compared their photocatalytic HERs with those of corresponding D–A1 and D–A2 systems [81,82]. the D–A1 (Py-ThTh) polymer exhibited an HER of 1874 μmol g^{-1} h^{-1}, while the D–A2 (PyDOBT-1) system achieved a significantly higher rate of 12,986 μmol g^{-1} h^{-1}. In contrast, the D–A–A structured polymers demonstrated even greater activity, underscoring the synergistic effect of incorporating two electron-accepting units within the conjugated framework. This progressive enhancement in photocatalytic performance—from individual monomers to D–A1, D–A2, and finally D–A1–A2 systems—highlights the crucial role of molecular design in facilitating efficient light harvesting, charge separation, and H_2 evolution. These results collectively confirm that the D–A1–A2 architecture offers a superior pathway for optimizing polymer photocatalysts for visible-light-driven H_2 production.

The photocatalytic H_2 evolution performance of CMPs is intricately linked to their internal structural characteristics, including internal disorder, surface defects, and the spatial arrangement of D and A units. Adjusting the FMR during synthesis can significantly influence these structural aspects, thereby affecting photocatalytic efficiency. It was suggested that rigidification might be a general strategy for improving photocatalytic H_2 evolution in organic polymers, where the optical gap can be tuned by composition [83]. Internal disorder in CMPs, often resulting from irregular monomer arrangements or non-ideal polymerization conditions, can disrupt π-conjugation pathways. This disruption hampers effective charge transport and increases the likelihood of

electron-hole recombination, leading to reduced photocatalytic activity. For instance, studies have shown that CMPs with higher degrees of structural order exhibit enhanced charge mobility and, consequently, better photocatalytic performance [84]. The PyTzTzSO-1 with the smallest FMR (1.0:3.0:1.0) had smaller chains, which gives rise to decreased flexibility, increased rigidity, and reduced internal disorder of the resultant polymer, leading to great photocatalytic activity. On the other hand, by increasing the FMR in the PyTzTzSO-2 and the PyTzTzSO-3, the chains will be longer, the flexibility will increase, the rigidity will decrease, the internal disorder will expand, and hence the photocatalytic efficiency will be lower.

In addition, surface defects, such as vacancies or irregularities on the polymer surface, can act as recombination centers for photogenerated charge carriers. These defects trap electrons or holes, preventing them from participating in the photocatalytic reaction. controlling the FMR can influence the formation of such defects; a balanced ratio promotes uniform polymer growth, minimizing defect formation [84]. Moreover, polymers displaying high crystallinity, and thus few defects, can suppress recombination events as the charges can separate more easily and have higher mobility [85–87]. A reverse relationship exists between the chain flexibility within a polymer and its crystallinity. When the chain is long, the flexibility will be high, the crystallinity will be low, the surface defects will increase, and thus the photocatalytic performance will be poor, as observed in the PyTzTzSO-3 with the highest FMR (1.0:5.0:7.0).

The spatial distance between donor and acceptor units within CMPs is critical for efficient charge separation. An optimal arrangement facilitates effective electron transfer from donor to acceptor, reducing recombination rates. Adjusting the monomer feed ratio allows for tuning this spatial arrangement. For example, incorporating an alkyne bridge between D and A units has enhanced charge separation efficiency, improving hydrogen evolution rates [84]. However, the PyTzTzSO-1 with balanced FMR resulted in a polymer with moderate internal order and minimal surface defects. The optimized D-A spacing facilitated efficient charge separation, leading to the highest HER among the three polymers. The increased A content in the PyTzTzSO-2 led to extended D-A distances, which hindered effective charge transfer. Additionally, the imbalance introduced more structural disorders, resulting in a moderate HER. The further increase in A content in the PyTzTzSO-3 exacerbated internal disorder and surface defects. The excessive D-A distance significantly impeded charge separation, leading to the lowest HER among the three polymers studied.

In general, the researchers considered library 6354 copolymers, synthesized more than 170 polymers, and tested them for photocatalytic H_2 generation. The results confirmed that there is a weak link between the efficiency of photocatalytic HERs and every property of the polymer, which supports the opinion that the factors affecting photocatalytic HERs are multifactorial properties that are related to many mutually independent factors [88,89].

3.7. Density Functional Theory (DFT) calculations

We expand the study by turning to the Kohn-Sham Density Functional Theory to gain further insights into the D-A CMP. We performed first-principles calculations within the Gaussian software package [90]. Structure optimizations were carried out within the DFT framework. The B3LYP exchange–correlation functional [91–93] and the 6-31G basis set [94] were employed. Additionally, the Grimme D3 dispersion correction [95] was added. Full structural relaxation was performed until all forces were less than 0.001 eV/ Å. Table S4 gives a summary of the computational results. We work with different models of the CMP that contain different ratios of D and A moieties covering the length of the models between 3.1 ($C_{44}H_{24}N_2O_2S_3$), 5.3 ($C_{72}H_{38}N_4O_4S_6$), and 7.5 nm ($C_{100}H_{52}N_6O_6S_3$). Note that the CMP models have one donor moiety and different amounts of acceptor-pair moieties resulting in different D-A ratios, i.e. D-A1-A2, D-A1-A2-A1-A2, and D-A1-A2-A1-A2-A1-A2.

Regarding the HER process, the different stages of the reaction path are accessible through adsorption simulations. The adsorption of H and H_2 was sampled with 40 random initial structures with distances between adsorbates and the CMP models ($C_{44}H_{24}N_2O_2S_3$, $C_{72}H_{38}N_4O_4S_6$, and $C_{100}H_{52}N_6O_6S_3$) between 1.2 and 4.0 Å for each of the CMP models, i.e. a total of 240 adsorption calculations with full structural relaxation. The adsorption energies $\boldsymbol{E_{ad}}$ were calculated with respect to the separated constituents, i.e., a CMP and either H_2 or H, referred to as $\boldsymbol{E_{CMP}}$ and $\boldsymbol{E_H}$ or $\boldsymbol{E_{H2}}$, according to $\boldsymbol{E_{ad,CMP+H/H2} = E_{CMP+H/H2} - E_{CMP} - E_{H/H2}}$. The adsorption energies appear to be independent of the size of the CMP model. H_2 and H adsorbs exothermally with about 110 meV and 90 meV binding energy, respectively. Overall, the observed energy differences between different adsorption sites showed only a dependence on the local chemical environment, i.e. the binding strength was identical at similar binding sites independently of in the polymer chain. The binding of H_2 and H happened on the electronegative sulfone groups with binding distances of 2.441 and 2.388 Å, respectively (Figs. S31 and S32).

We extend the computational model by including two polymer chains weakly interacting with each other. This allows investigate the impact of the local chemical environment on the interaction of the polymers with H_2, and to further analysis possible effects thereof. Two models (Fig. S33), one with parallel polymer strains ($2 \times C_{44}H_{24}N_2O_2S_3$) and an arrangement with non-parallel initial arrangement. Note that geometry optimization shows a preferential intermolecular interaction between positively and negatively charged moieties, e.g., between sulfone groups and benzene moieties, and between thiazole and benzene moieties. This could indicate the presence of built-in microscopic electric fields which were recently presented to be beneficial migration of photogenerated charge carriers for catalytic activities in polymers [96]. The parallel model is energetically slightly preferred by about 0.7 eV due to the increased van der Waals interactions by π-π stacking. Testing different favorable H_2 adsorption sites, e.g., in the vicinity of sulfone groups, we note a slight increase in H_2 binding strength by about 25 meV, which is constituted by the additional van der Waals interaction between H_2 and the benzene moieties of the neighboring polymer chain. However, the binding distance of H_2 to the polymer at the sulfone group increases to 2.451 Å indicating competing attraction among the polymers, while the bond length in H_2 remains at 0.746 Å (about 0.003 Å larger than in isolated H_2). Henceforth, it appears that the leading interactions between H_2 and isolated polymer chains remain valid even for polymer aggregate, while the arrangement of D-A CMP is likely to benefit from built-in electric fields which may enhance the migration process of photogenerated charge carriers.

Among the different single polymer chain models, HOMO and LUMO energy levels are rather similar. The smaller models have their HOMO at −5.40 eV. The positions of the LUMO are more affected by the structural differences. The LUMO of the smaller models is at −2.63 and the one of the larger models at −2.91 eV that equates to an energy gap contraction of 0.28 eV from a HOMO–LUMO gap of 2.77 eV–2.49 eV for the larger model. It should be noted that the energy gap of the larger model is closer to the ideal value of 2.37 eV, and that the changes with increasing size are monotonic. Furthermore, the here reported energy gaps are larger than the experimental values; a DFT untypical outcome which can be explained with possible impacts from the CMP aggregate phase. Nonetheless, trends observed, and conclusions drawn from the computational results should be valid. Other electronic properties (given in a Tab. S4) display similar trends. The vertical electron affinity and the vertical ionization potential range from 1.67 to 2.35 eV and from 6.48 to 6.22 eV respectively. This indicates a greater size-dependent on properties related to the removal or addition of an electron on the CMPs, and potentially equally applicable for the charge transfer processes during catalytic processes. Likewise, the overlap of the HOMO and LUMO of CMPs with different sizes given in Fig. S31 also indicates a potential impact on the excitonic state under photon adsorption and charge transfer performance.

4. Conclusion

In summary, D-A1-A2 type CMPs enable enhanced modulation of photophysical properties and exhibit superior charge separation and photocatalytic efficiency compared to D-A CMPs. Thus, we successfully developed a set of D-A1-A2 ternary polymer photocatalysts through a statistical polymerization protocol by regulating the FMR to address the impact of molecular engineering on the energy gap, charge separation kinetics, and photocatalytic performance. The synthesized polymers possessed considerable porosities (reaching 251 $m^2\ g^{-1}$), accessible morphologies, high hydrophilicities (CA up to 53.5°), and suitable Eg (up to 2.43 eV). The comparative study of the three CMPs showed that the PyTzTzSO-1 polymer with 1.0:3.0:1.0 FMR displayed the top photocatalytic efficiency with an HER of 39.11 mmol $h^{-1}\ g^{-1}$ under UV/Vis light irradiation. Interestingly, it displayed a greater AQY value of 51.31 % at 420 nm, which is comparable to the state-of-the-art values. The supreme photocatalytic performance of the PyTzTzSO-1 compared to the others was basically due to its capability to promote photoelectron transfer and suppress electron-hole recombination. These results not only provide auspicious CMPs photocatalysts with outstanding photocatalytic performance for HER but also highlight the remarkable influence of the rational structure and chemical composition on improving the photocatalytic activity of D-A CMPs photocatalysts.

CRediT authorship contribution statement

Ahmed F. Saber: Writing – original draft, Methodology, Investigation, Conceptualization. **Huei-Ting Liao:** Writing – original draft, Software, Methodology, Data curation, Conceptualization. **Pei-Jung Li:** Data curation, Methodology, Validation. **Ya-Fan Chen:** Writing – original draft, Software. **Levannie Mabuti:** Writing – original draft, Software. **Shiao-Wei Kuo:** Formal analysis, Resources, Validation. **Johann Lüder:** Writing – original draft, Software, Supervision, Software. **Ahmed F.M. EL-Mahdy:** Formal analysis, Resources, Validation, Supervision, Writing – original draft.

Declaration of competing interest

The authors declare that they have no known competing financial interests or personal relationships that could have appeared to influence the work reported in this paper.

Acknowledgements

This study was supported financially by the National Science and Technology Council, Taiwan, under contract NSTC 112-2221-E-110-005-MY3.

Appendix A. Supplementary data

Supplementary data to this article can be found online at https://doi.org/10.1016/j.jcis.2025.138156.

Data availability

Data will be made available on request.

References

[1] M. Gray, S. Sundaresan, B. Udomchaiporn, S. Lavelle, L. Chau, Carbon Tracker Initiative, London, 2020.
[2] I. Staffell, D. Scamman, A. Velazquez Abad, P. Balcombe, P.E. Dodds, P. Ekins, N. Shah, K.R. Ward, The role of hydrogen and fuel cells in the global energy system, energy, Environ. Sci. 12 (2019) 463–491.
[3] F. Dawood, M. Anda, G.M. Shafiullah, Hydrogen production for energy: an overview, Int. J. Hydrogen Energy 45 (2020) 3847–3869.
[4] X.J. Chen, J. Wang, Y.Q. Chai, Z.J. Zhang, Y.F. Zhu, Efficient photocatalytic overall water splitting induced by the giant internal electric field of a g-C_3N_4/rGO/PDIP Z-scheme heterojunction, Adv. Mater. 33 (2021) 2007479.
[5] Q. Wang, K. Domen, Particulate photocatalysts for light-driven water splitting: mechanisms, challenges, and design strategies, Chem. Rev. 120 (2020) 919–985.
[6] S.A. Shah, I. Khan, A. Yuan, MoS_2 as a co-catalyst for photocatalytic hydrogen production: a mini review, Molecules 27 (2022) 3289.
[7] Y. Fang, Y. Hou, X. Fu, X. Wang, Semiconducting polymers for oxygen evolution reaction under light illumination, Chem. Rev. 122 (2022) 4204–4256.
[8] Z. Chen, L. Guo, L. Pan, T. Yan, Z. He, Y. Li, C. Shi, Z.F. Huang, X. Zhang, J.J. Zou, Advances in oxygen evolution electrocatalysts for proton exchange membrane water electrolyzers, Adv. Energy Mater. 12 (2022) 2103670.
[9] R.S. Sprick, J.X. Jiang, B. Bonillo, S. Ren, T. Ratvijitvech, P. Guiglion, M. A. Zwijnenburg, D.J. Adams, A.I. Cooper, Tunable organic photocatalysts for visible-light-driven hydrogen evolution, J. Am. Chem. Soc. 137 (2015) 3265–3270.
[10] V.S. Vyas, F. Haase, L. Stegbauer, G. Savasci, F. Podjaski, C. Ochsenfeld, B. V. Lotsch, A tunable azine covalent organic framework platform for visible light-induced hydrogen generation, Nat. Commun. 6 (2015) 8508.
[11] S. Wu, Y. Pan, H. Lin, L. Li, X. Fu, J. Long, Crystalline covalent organic frameworks with tailored linkages for photocatalytic H_2 evolution, ChemSusChem 14 (2021) 4958–4972.
[12] P. Verma, J.J.M. Le Brocq, R. Raja, Rational design and application of covalent organic frameworks for solar fuel production, Molecules 26 (2021) 4181.
[13] B. Wang, G.M. Biesold, M. Zhang, Z.Q. Lin, Amorphous inorganic semiconductors for the development of solar cell, photoelectrocatalytic and photocatalytic applications, Chem. Soc. Rev. 50 (2021) 6914–6949.
[14] C. Shu, C.Z. Han, X.Y. Yang, C. Zhang, Y. Chen, S.J. Ren, F. Wang, F. Huang, J. X. Jiang, Boosting the photocatalytic hydrogen evolution activity for D-pi-a conjugated microporous polymers by statistical copolymerization, Adv. Mater. 33 (2021) 2008498.
[15] T. Zhang, Y. Qian, H. Gao, Z.C. Huang-Fu, J.B. Brown, Y. Rao, Surface states for photoelectrodes of gallium phosphide (GaP) with surface-specific electronic spectra and phase measurements, J. Phys. Chem. C 126 (2022) 6761–6772.
[16] H. Wang, H. Wang, Z. Wang, L. Tang, G. Zeng, P. Xu, M. Chen, T. Xiong, C. Zhou, X. Li, D. Huang, Y. Zhu, Z. Wang, J. Tang, Covalent organic framework photocatalysts: structures and applications, Chem. Soc. Rev. 49 (2020) 4135–4165.
[17] C.Z. Han, P.H. Dong, H.R. Tang, P.Y. Zheng, C. Zhang, F. Wang, F. Huang, J. X. Jiang, Realizing high hydrogen evolution activity under visible light using narrow band gap organic photocatalysts, Chem. Sci. 12 (2021) 1796–1802.
[18] T. Bhoyar, D.J. Kim, B.M. Abraham, S. Tonda, N.R. Manwar, D. Vidyasagar, S. S. Umare, Tailoring photoactivity of polymeric carbon nitride via donor-pi-acceptor network, Appl. Catal. B Environ. 310 (2022) 121347.
[19] Z.L. Li, H. Fang, Z.P. Chen, W.X. Zou, C.X. Zhao, X.F. Yang, Regulating donor acceptor interactions in triazine-based conjugated polymers for boosted photocatalytic hydrogen production, Appl. Catal. B Environ. 312 (2022) 121374.
[20] J.H. Wang, A.E. Hassan, A.M. Elewa, A.F.M. EL-Mahdy, Donor–acceptor hetero[6] radialene-based three-dimensional covalent organic frameworks for organic pollutant adsorption, photocatalytic degradation, and hydrogen production activity, J. Mater. Chem. A 12 (2024) 14005–14021.
[21] Y.Z. Xiao, A.A.K. Mohammed, S.W. Kuo, A.F.M. EL-Mahdy, Innovative β-ketoenamine-linked covalent organic frameworks: tailored D1-a-D2-A structure for highly efficient photocatalytic degradation of organic pollutants, Sep. Purif. Technol. 356 (2025) 129950.
[22] B. Chao, A. Santhana Krishna Kumar, M. Rashad, F.C. Chang, W.L. Tseng, P. V. Pham, W.C. Lin, K.I. Aly, R.H. Lee, A.F.M. EL-Mahdy, Donor–Acceptor pyrrolo [3,2-b] pyrrolyl-and dibenzothiophene-containing microporous polymeric frameworks for photocatalytic organic pollutant degradation, ACS Appl. Polym. Mater. 7 (2025) 998–1011.
[23] A.F. Saber, Y.F. Chen, L. Mabuti, S.V. Chaganti, S.U. Sharma, J. Lüder, J.T. Lee, S. W. Kuo, A.F.M. EL-Mahdy, Engineering carbonyl-rich conjugated microporous polymers with a pyrene-4,5,9,10-tetraone building block as highly efficient and stable electrodes for energy storage, Mater. Adv. 6 (2025) 607.
[24] S. Das, P. Heasman, T. Ben, S. Qiu, Porous organic materials: strategic design and structure–function correlation, Chem. Rev. 117 (2017) 1515–1563.
[25] A.F. Saber, A.F.M. EL-Mahdy, (E)-1, 2-Diphenylethene-based conjugated nanoporous polymers for a superior adsorptive removal of dyes from water, New J. Chem. 45 (2021) 21834–21843.
[26] S.H. Kang, A. Jeong, H.R. Lee, J.H. Oh, C. Yang, Bioderived and eco-friendly solvent-processed high-mobility ambipolar plastic transistors through controlled irregularity of the polymer backbone, Chem. Mater. 31 (2019) 3831–3839.
[27] A.F. Saber, K.Y. Chen, A.F.M. EL-Mahdy, S.W. Kuo, Designed azo-linked conjugated microporous polymers for CO_2 uptake and removal applications, J. Polym. Res. 28 (2021) 1–12.
[28] K.Y. Lin, A.F.M. EL-Mahdy, Covalent triazine frameworks based on triphenylpyridine building block for high-performance supercapacitor and selective CO_2 capture, Mater. Chem. Phys. 281 (2022) 125850.
[29] A.F. Saber, C.C. Chueh, M. Rashad, S.W. Kuo, A.F.M. EL-Mahdy, Thiazolyl-linked conjugated microporous polymers for enhancement adsorption and photocatalytic degradation of organic dyes from water, Mater. Today Sustain. 23 (2023) 100429.
[30] V. Lakshmi, C.H. Liu, M.R. Rao, Y. Chen, Y. Fang, A. Dadvand, E. Hamzehpoor, Y. Sakai-Otsuka, R.S. Stein, D.F. Perepichka, A two-dimensional poly (-azatriangulene) covalent organic framework with semiconducting and paramagnetic states, J. Am. Chem. Soc. 142 (2020) 2155–2160.
[31] A.F. Saber, S.U. Sharma, J.T. Lee, A.F.M. EL-Mahdy, S.W. Kuo, Carbazole-conjugated microporous polymers from Suzuki-Miyaura coupling for supercapacitors, Polymer 254 (2022) 125070–125076.

[32] R. Sun, S. Feng, B. Zhou, Z. Chen, D. Wang, H. Liu, Flexible cyclosiloxane-linked fluorescent porous polymers for multifunctional chemical sensors, ACS Macro Lett. 9 (2020) 43–48.

[33] J.H. Wang, C.C. Chang, Z.W. Zhang, A.F.M. EL-Mahdy, Facile metal-free synthesis of pyrrolo[3,2-b]pyrrolyl-based conjugated microporous polymers for highperformance photocatalytic degradation of organic pollutants, Polym. Chem. 13 (2022) 5300–5308.

[34] M.G. Kotp, C.L. Chang, A.F.M. EL-Mahdy, Tetraphenyl-p-phenylenediamine-based tunable conjugated microporous polymers: adsorption and photodegradation of hazardous dyestuff in aqueous environments, J. Water Process Eng. 53 (2023) 103675.

[35] W. Li, X. Huang, T. Zeng, Y.A. Liu, W. Hu, H. Yang, Y.B. Zhang, K. Wen, Thiazolo [5,4-d]thiazole-based donor–acceptor covalent organic framework for sunlight-driven hydrogen evolution, Angew. Chem. Int. Ed. 60 (2021) 1869–1874.

[36] Y.H. Kim, N. Kim, J.M. Seo, J.P. Jeon, H.J. Noh, D.H. Kweon, J. Ryu, J.B. Baek, Benzothiazole-based covalent organic frameworks with different symmetrical combinations for photocatalytic CO_2 conversion, Chem. Mater. 33 (2021) 8705–8711.

[37] C. Shu, C. Han, X. Yang, C. Zhang, Y. Chen, S. Ren, F. Wang, F. Huang, J.X. Jiang, Boosting the photocatalytic hydrogen evolution activity for D–π–A conjugated microporous polymers by statistical copolymerization, Adv. Mater. 33 (2021) 2008498.

[38] S. Han, Z. Li, S. Ma, Y. Zhi, H. Xia, X. Chen, X. Liu, Bandgap engineering in benzotrithiophene-based conjugated microporous polymers: a strategy for screening metal-free heterogeneous photocatalysts, J. Mater. Chem. A 9 (2021) 3333–3340.

[39] W. Zhang, L. Chen, S. Dai, C. Zhao, C. Ma, L. Wei, M. Zhu, S.Y. Chong, H. Yang, L. Liu, S. Luo, M. Yu, Y. Xu, X.W. Zhu, Q. Zhu, S. An, R.S. Sprick, M.A. Little, X. Wu, S. Jiang, Y. Wu, Y.B. Zhang, H. Tian, W.H. Zhu, A.I. Cooper, Reconstructed covalent organic frameworks, Nature 604 (2022) 72–79.

[40] T. Zhou, L. Wang, X. Huang, J. Unruangsri, H. Zhang, R. Wang, Q. Song, Q. Yang, W. Li, C. Wang, K. Takahashi, H. Xu, J. Guo, PEG-stabilized coaxial stacking of two-dimensional covalent organic frameworks for enhanced photocatalytic hydrogen evolution, Nat. Commun. 12 (2021) 3934.

[41] C. Han, P. Dong, H. Tang, P. Zheng, C. Zhang, F. Wang, F. Huang, J.X. Jiang, Realizing high hydrogen evolution activity under visible light using narrow band gap organic photocatalysts, Chem. Sci. 12 (2020) 1796–1802.

[42] C. Han, S. Xiang, S. Jin, L.W. Luo, C. Zhang, C. Yan, J.X. Jiang, Linear multiple-thiophene-containing conjugated polymer photocatalysts with narrow band gaps for achieving ultrahigh photocatalytic hydrogen evolution activity under visible light, J. Mater. Chem. A 10 (2022) 5255–5261.

[43] L. Li, W.Y. Lo, Z. Cai, N. Zhang, L. Yu, Donor–acceptor porous conjugated polymers for photocatalytic hydrogen production: the importance of acceptor comonomer, Macromolecules 49 (2016) 6903–6909.

[44] G. Li, Z. Xie, S. Chai, X. Chen, X. Wang, A facile one-step fabrication of holey carbon nitride nanosheets for visible-light-driven hydrogen evolution, Appl. Catal. b: Environ. 283 (2021) 119637.

[45] Z. Xie, W. Wang, X. Ke, X. Cai, X. Chen, S. Wang, W. Lin, X. Wang, A heptazine-based polymer photocatalyst with donor-acceptor configuration to promote exciton dissociation and charge separation, Appl. Catal. b: Environ. 325 (2023) 122312.

[46] L.R. Ahmed, A.F.M. EL-Mahdy, C.T. Pan, S.W. Kuo, A water-soluble copper immobilized covalent organic framework functioning as an "OFF–ON" fluorescent sensor for amino acids, Mater. Adv. 2 (2021) 4617–4629.

[47] Z.A. Lan, M. Wu, Z. Fang, X. Chi, X. Chen, Y. Zhang, X. Wang, A fully coplanar donor–acceptor polymeric semiconductor with promoted charge separation kinetics for photochemistry, Angew. Chem. Int. Ed. 60 (2021) 16355–16359.

[48] A.F. Saber, A.M. Elewa, H.H. Chou, A.F.M. EL-Mahdy, Donor to acceptor charge transfer in carbazole-based conjugated microporous polymers for enhanced visible-light-driven photocatalytic water splitting, ChemCatChem 15 (2023) e202201287.

[49] A.F. Saber, A.M. Elewa, H.H. Chou, A.F.M. EL-Mahdy, Donor-acceptor carbazole-based conjugated microporous polymers as photocatalysts for visible-light-driven H_2 and O_2 evolution from water splitting, Appl. Catal. b: Environ. 316 (2022) 121624–121633.

[50] F.T. Yu, Z.Q. Zhu, S.P. Wang, Y.K. Peng, Z.Z. Xu, Y. Tao, J.B. Xiong, Q.W. Fan, F. Luo, Tunable perylene-based donor-acceptor conjugated microporous polymer to significantly enhance photocatalytic uranium extraction from seawater, Chem. Eng. J. 412 (2021) 127558.

[51] Z. Zhong, X. Xia, X. Yang, N. Li, J. He, D. Chen, P. Gu, Q. Xu, J. Lu, Metal-free modification of porphyrin-based porous organic polymers for effective photocatalytic degradation of bisphenol a in water, Sep. Purif. Tech. 301 (2022) 121981.

[52] H. Zhao, Y. Dong, P. Sun, Y. Bai, C. Ru, X. Wu, Z. Li, X. Han, J. Wu, X. Pan, Effect of D/A ratio on photocatalytic hydrogen evolution performance of conjugated polymer photocatalysts, ACS Appl. Energy Mater. 5 (4) (2022) 4631–4640.

[53] C. Han, S. Xiang, P. Xie, P. Dong, C. Shu, C. Zhang, J.X. Jiang, A Universal strategy for boosting hydrogen evolution activity of polymer photocatalysts under visible light by inserting a narrow-band-gap spacer between donor and acceptor, Adv. Funct. Mater. 32 (2022) 2109423.

[54] C. Shu, C. Han, X. Yang, C. Zhang, Y. Chen, S. Ren, F. Wang, F. Huang, J.X. Jiang, Boosting the photocatalytic hydrogen evolution activity for D–π–A conjugated microporous polymers by statistical copolymerization, Adv. Mater. 33 (2021) 2008498.

[55] P. Xie, C. Han, S. Xiang, S. Jin, M. Ge, C. Zhang, J.X. Jiang, Toward high-performance dibenzo[g,p]chrysene-based conjugated polymer photocatalysts for photocatalytic hydrogen production through donor-acceptor-acceptor structure design, Chem. Eng. J. 459 (2023) 141553.

[56] T. Banerjee, F. Podjaski, J. Kroger, B.P. Biswal, B.V. Lotsch, Polymer photocatalysts for solar-to-chemical energy conversion, Nat. Rev. Mater. 6 (2020) 168–190.

[57] A. Giri, Y. Khakre, G. Shreeraj, T.K. Dutta, S. Kundu, A. Patra, The order–disorder conundrum: a trade-off between crystalline and amorphous porous organic polymers for task-specific applications, J. Mater. Chem. A 10 (2022) 17077–17121.

[58] S.H. Xiang, C.Z. Han, C. Shu, C. Zhang, J.X. Jiang, Structure evolution of thiophene-containing conjugated polymer photocatalysts for high-efficiency photocatalytic hydrogen production, Sci. China Mater. 65 (2022) 422–430.

[59] F.T. Yu, Z.Q. Wang, S.C. Zhang, W.J. Wu, H.N. Ye, H.R. Ding, X.Q. Gong, J.L. Hua, Construction of polymeric carbon nitride and dibenzothiophene dioxide-based intramolecular donor-acceptor conjugated copolymers for photocatalytic H_2 evolution, Nanoscale Adv. 3 (2021) 1699–1707.

[60] L.P. Xu, Y. Zhao, Z.F. Li, J.H. Wu, J.W. Cui, B.N. Tian, Y.C. Wu, Y. Tian, π-d electron-coupled PBDIT/CdS heterostructure enables hole extraction for efficient photocatalytic hydrogen production, ACS. Appl. Mater. Inter. 14 (2022) 25278–25287.

[61] M. Samal, S. Valligatla, N.A. Saad, M. Rao, D. Rao, R. Sahu, B.P. Biswal, A thiazolo [5,4-d]thiazole-bridged porphyrin organic framework as a promising nonlinear optical material, Chem. Commun. 55 (2019) 11025–11028.

[62] A. Dessì, M. Calamante, A. Mordini, M. Peruzzini, A. Sinicropi, R. Basosi, F. Fabrizi de Biani, M. Taddei, D. Colonna, A. Carlo, G. Reginato, L. Zani, Thiazolo[5,4-d] thiazole-based organic sensitizers with strong visible light absorption for transparent, efficient and stable dye-sensitized solar cells, RSC Adv. 3 (2015) 32657–32668.

[63] Y.S. Kochergin, D. Schwarz, A. Acharjya, A. Ichangi, R. Kulkarni, P. Eliášov á, J. Vacek, J. Schmidt, A. Thomas, M.J. Bojdys, Exploring the "Goldilocks Zone" of semiconducting polymer photocatalysts by donor–acceptor interactions, Angew. Chem. Int. Ed. 57 (2018) 1–6.

[64] X. Gao, C. Shu, C. Zhang, W. Ma, S.B. Ren, F. Wang, Y. Chen, J.H. Zeng, J.X. Jiang, Substituent effect of conjugated microporous polymers on the photocatalytic hydrogen evolution activity, J. Mater. Chem. A 8 (2020) 2404–2411.

[65] L.P. Guo, Y.L. Niu, S. Razzaque, B.E. Tan, S.B. Jin, Design of D–A1–A2 covalent triazine frameworks via copolymerization for photocatalytic hydrogen evolution, ACS Catal. 9 (2019) 9438–9445.

[66] F. Li, X. Dai, L. Zhang, H. Wu, J. Li, J. Guo, Q. Yi, Triphenylamine promoted geometric structure adjusting of the novel macrocyclic structure D-π-a conjugated microporous polymers for photocatalytic hydrogen evolution, Fuel 370 (2024) 131812.

[67] F. Yu, Z. Zhu, S. Wang, J. Wang, Z. Xu, F. Song, Z. Dong, Z. Zhang, Novel donor-acceptor-acceptor ternary conjugated microporous polymers with boosting forward charge separation and suppressing backward charge recombination for photocatalytic reduction of uranium (VI), Appl. Catal. b: Environ. 301 (2022) 120819.

[68] J.S.M. Lee, A.I. Cooper, Advances in conjugated microporous polymers, Chem. Rev. 120 (2020) 2171–2214.

[69] Q. Sheng, X. Zhong, Q. Shang, Y.Y. Dong, J. Zhao, Y. Du, Y. Xie, Triazine-based conjugated microporous polymers with different linkage units for visible light–driven hydrogen evolution, Front. Chem. 10 (2022) 854018.

[70] W.Y. Huang, Z.Q. Shen, J.Z. Cheng, L.L. Liu, K. Yang, X.R. Chen, H.R. Wen, S. Y. Liu, C–H activation derived CPPs for photocatalytic hydrogen production excellently accelerated by a DMF cosolvent, J. Mater. Chem. A 7 (2019) 24222–24230.

[71] R.S. Sprick, C.M. Aitchison, E. Berardo, L. Turcani, L. Wilbraham, B.M. Alston, K. E. Jelfs, M.A. Zwijnenburg, A.I. Cooper, Maximising the hydrogen evolution activity in organic photocatalysts by co-polymerisation, J. Mater. Chem. A 6 (2018) 11994–12003.

[72] L. Tan, B. Tan, Hypercrosslinked porous polymer materials: design, synthesis, and applications, Chem. Soc. Rev. 46 (2017) 3322–3356.

[73] Y. Xu, S. Jin, H. Xu, A. Nagaia, D. Jiang, Conjugated microporous polymers: design, synthesis and application, Chem. Soc. Rev. 42 (2013) 8012–8031.

[74] C. Shu, C. Han, X. Yang, C. Zhang, Y. Chen, S. Ren, F. Wang, F. Huang, J.X. Jiang, Boosting the photocatalytic hydrogen evolution activity for D–π–A conjugated microporous polymers by statistical copolymerization, Adv. Mater. 33 (2021) 2008498.

[75] J. Chakraborty, I. Nath, S. Song, S. Mohamed, A. Khan, P.M. Heynderickx, F. Verpoort, Porous organic polymer composites as surging catalysts for visible-light-driven chemical transformations and pollutant degradation, J. Photochem. Photobiol. C: Photochem. Rev. 41 (2019) 100319.

[76] S. Bi, C. Yang, W. Zhang, J. Xu, L. Liu, D. Wu, X. Wang, Y. Han, Q. Liang, F. Zhang, Two-dimensional semiconducting covalent organic frameworks via condensation at arylmethyl carbon atoms, Nat. Commun. 10 (2019) 2467.

[77] W. Zhang, Z. Deng, J. Deng, C.T. Au, Y. Liao, H. Yang, Q. Liu, Regulating the exciton binding energy of covalent triazine frameworks for enhancing photocatalysis, J. Mater. Chem. A 10 (2022) 22419–22427.

[78] R. Liang, J. Luo, S. Lin, Z. Li, Z. Dong, Y. Wu, Y. Wang, X. Cao, C. Meng, F. Yu, Y. Liu, Z. Zhang, Boosting the photoreduction uranium activity for donor–acceptor–acceptor type conjugated microporous polymers by statistical copolymerization, Sep. Purif. Technol. 312 (2023) 123291.

[79] T. Banerjee, K. Gottschling, G. Savasci, C. Ochsenfeld, B.V. Lotsch, H_2 Evolution with covalent organic framework photocatalysts, ACS Energy Lett. 3 (2) (2018) 400–409.

[80] M. Rahman, H. Tian, T. Edvinsson, Revisiting the limiting factors for overall water-splitting on organic photocatalysts, Angew. Chem. Int. Ed. 59 (38) (2020) 16278–16293.

[81] Y. Zhao, W. Ma, Y. Xu, C. Zhang, Q. Wang, T. Yang, X. Gao, F. Wang, C. Yan, J. X. Jiang, Effect of linking pattern of dibenzothiophene-S,S-dioxide-containing

conjugated microporous polymers on the photocatalytic performance, Macromolecules 51 (23) (2018) 9502–9508.
[82] M.M. Samy, I.M.A. Mekhemer, M.G. Mohamed, M.H. Elsayed, K.H. Lin, Y.K. Chen, T.L. Wu, H.H. Chou, S.W. Kuo, Conjugated microporous polymers incorporating Thiazolo[5,4-d]thiazole moieties for Sunlight-Driven hydrogen production from water, Chem. Eng. J. 446 (3) (2022) 137158.
[83] R.S. Sprick, B. Bonillo, R. Clowes, P. Guiglion, N.J. Brownbill, B.J. Slater, F. Blanc, M.A. Zwijnenburg, D.J. Adams, A.I. Cooper, Visible-light-driven hydrogen evolution using planarized conjugated polymer photocatalysts, Angew. Chem. 128 (2016) 1824–1828.
[84] M.G. Mohamed, M.H. Elsayed, C.J. Li, A.E. Hassan, I.M.A. Mekhemer, A.F. Musa, M.K. Hussien, L.C. Chen, K.H. Chen, H.H. Chou, S.W. Kuo, Reticular design and alkyne bridge engineering in donor–π–acceptor type conjugated microporous polymers for boosting photocatalytic hydrogen evolution, J. Mater. Chem. A 12 (2024) 7693–7710.
[85] S. Zhu, D. Wang, Photocatalysis: basic principles, diverse forms of implementations and emerging scientific opportunities, Adv. Energy Mater. 7 (2017) 1700841.
[86] X. Yang, D. Wang, Photocatalysis: from Fundamental Principles to Materials and applications, ACS Appl. Energy Mater. 1 (2018) 6657–6693.
[87] J. Yu, L. Zhang, L. Wang, B. Zhu, S-scheme Heterojunction Photocatalysts Fundamentals and Applications, Interface Science and Technology, Elsevier, Amsterdam, 1st edn, 2023, ch. 1, 35, 1–35.
[88] Y. Bai, L. Wilbraham, B.J. Slater, M.A. Zwijnenburg, R.S. Sprick, A.I. Cooper, Accelerated discovery of organic polymer photocatalysts for hydrogen evolution from water through the integration of experiment and theory, J. Am. Chem. Soc. 141 (2019) 9063–9071.
[89] S. Luo, Z. Zeng, G. Zeng, Z. Liu, R. Xiao, P. Xu, H. Wang, D. Huang, Y. Liu, B. Shao, Q. Liang, D. Wang, Q. He, L. Qin, Y. Fu, Recent advances in conjugated microporous polymers for photocatalysis: designs, applications, and prospects, J. Mater. Chem. A 8 (2020) 6434.
[90] M. J. Frisch, G. W. Trucks, H. B. Schlegel, G. E. Scuseria, M. A. Robb, J. R. Cheeseman, G. Scalmani, V. Barone, G. A. Petersson, H. Nakatsuji, X. Li, M. Caricato, A. V. Marenich, J. Bloino, B. G. Janesko, R. Gomperts, B. Mennucci, H. P. Hratchian, J. V. Ortiz, A. F. Izmaylov, J. L. Sonnenberg, D. Williams-Young, F. Ding, F. Yupparini, F. Egidi, J. Goings, B. Peng, A. Petrone, T. Henderson, D. Ranasinghe, V. G. Zakrzewski, J. Gao, N. Rega, G. Zheng, W. Liang, M. Hada, M. Ehara, K. Toyota, R. Fukuda, J. Hasegawa, M. Ishida, T. Nakajima, Y. Honda, O. Kitao, H. Nakai, T. Vreven, K. Throssell, J. A. Montgomery Jr., J. E, Peralta, F. Ogliaro, M. J. Bearpark, J. J. J. Heyd, E. N. Brothers, K. N. Kudin, V. N. Staroverov, T. A. Keith, R. Kobayashi, J. Normand, K. Raghavachari, A. P. Rendell, J. C. Burant, S. S. Iyengar, J. Tomasi, M. Cossi, J. M. Millam, M. Klene, C. Adamo, R. Cammi, J. W. Ochterski, R. L. Martin, K. Morokuma, O. Farkas, J. B. Foresman, D. J. Fox, Gaussian, Inc., Wallingford CT (2016) GaussView 5.0. Wallingford, E.U.A.
[91] A.D. Becke, Density functional thermochemistry. I. the effect of the exchange only gradient correction, J. Chem. Phys. 96 (1992) 2155–2160.
[92] S.H. Vosko, L. Wilk, M. Nusair, Development of the Colle- Salvetti correlation-energy formula into a functional of the electron density, Can. J. Phys. 58 (1980) 1200–1211.
[93] P.J. Stephens, F.J. Devlin, C.F. Chabalowski, M.J. Frisch, Ab initio calculation of vibrational absorption and circular dichroism spectra using density functional force fields, J. Phys. Chem. 98 (1994) 11623–11627.
[94] R. Ditchfield, W.J. Hehre, J.A. Pople, Self-consistent molecular-orbital methods. ix. an extended gaussian-type basis for molecular-orbital studies of organic molecules, J. Chem. Phys. 54 (1971) 724–728.
[95] S. Grimme, J. Antony, S. Ehrlich, H. Krieg, A consistent and accurate ab initio parametrization of density functional dispersion correction (DFT-D) for the 94 elements H-Pu, J. Chem. Phys. 132 (2010) 154104.
[96] Y. Sheng, W. Li, L. Xu, Y. Zhu, High photocatalytic oxygen evolution via strong built-in electric field induced by high crystallinity of perylene imide supramolecule, Adv. Mater. 34 (10) (2022) 2102354.